



Curvilinear Kirigami Skins Let Soft Bending Actuators Slither Faster

Callie Branyan^{1,2*}, Ahmad Rafsanjani^{3,4}, Katia Bertoldi⁴, Ross L. Hatton¹ and Yiğit Mengüç^{1,5}

¹Collaborative Robotics and Intelligent Systems Institute, Oregon State University, Corvallis, OR, United States, ²Sandia National Laboratories, Albuquerque, NM, United States, ³Center for Soft Robotics, SDU Biorobotics, University of Southern Denmark, Odense, Denmark, ⁴John A. Paulson School of Engineering and Applied Sciences, Harvard University, Cambridge, MA, United States, ⁵Meta Reality Laboratory—Research, Redmond, WA, United States

The locomotion of soft snake robots is dependent on frictional interactions with the environment. Frictional anisotropy is a morphological characteristic of snakeskin that allows snakes to engage selectively with surfaces and generate propulsive forces. The prototypical slithering gait of most snakes is lateral undulation, which requires a significant lateral resistance that is lacking in artificial skins of existing soft snake robots. We designed a set of kirigami lattices with curvilinearly-arranged cuts to take advantage of in-plane rotations of the 3D structures when wrapped around a soft bending actuator. By changing the initial orientation of the scales, the kirigami skin produces high lateral friction upon engagement with surface asperities, with lateral to cranial anisotropic friction ratios above 4. The proposed design increased the overall velocity of the soft snake robot more than fivefold compared to robots without skin.

Keywords: soft robotics, kirigami, bioinspiration, biorobotics, mechanical design, mechanical metamaterials, locomotion

1 INTRODUCTION

Soft robots and limbless animals must break symmetry to achieve locomotion—through changing the shapes of their bodies and through the interaction of their skin with environments. Soft robots are particularly well suited for massive shape changes, but these changes result in large material deformations that make the attachment of skins challenging. Looking for existence proofs in nature to address this gap, we find snakes combine a malleable body coupled with specialized skins. Among snakes, lateral undulation is a typical gait strategy to leverage the combined benefits of their body and skin. As a result, snakes exist in nearly all ecological niches, from aquatic, terrestrial, to arboreal. To achieve undulatory locomotion, snakes propagate a body wave from head to tail (Gans, 1962) and their scales engage with asperities in the environmental surfaces resulting in necessary frictional anisotropy (Hu et al., 2009). Thus, any synthetic skin applied to snake-like robots must replicate the same ratio of lateral to longitudinal friction while permitting the body to slither.

Snakes primarily rely on undulatory locomotion to navigate through complex terrains. Rigid snake robots performing lateral undulation have been widely developed, but since they often use wheels to generate lateral forces (Hirose, 1993; Crespi and Jan Ijspeert, 2006), they lack the compliance of biological snakes. Soft snake robots performing lateral undulation have been developed to increase the deformability of the robot through the incorporation of soft materials (Onal and Rus, 2013; Branyan et al., 2017). There is biological evidence that lateral reaction forces are necessary for generating propulsive forces during undulatory locomotion (Hu et al., 2009) with measured lateral to longitudinal friction anisotropy values that can reach up to about 2:1 (Gray and

OPEN ACCESS

Edited by:

Michael Wehner,
University of Wisconsin-Madison,
United States

Reviewed by:

Hongbin Fang,
Fudan University, China
Jie Yin,
North Carolina State University,
United States

*Correspondence:

Callie Branyan
cabrany@sandia.gov

Specialty section:

This article was submitted to
Soft Robotics,
a section of the journal
Frontiers in Robotics and AI

Received: 09 February 2022

Accepted: 15 April 2022

Published: 03 May 2022

Citation:

Branyan C, Rafsanjani A, Bertoldi K,
Hatton RL and Mengüç Y (2022)
Curvilinear Kirigami Skins Let Soft
Bending Actuators Slither Faster.
Front. Robot. AI 9:872007.
doi: 10.3389/frobt.2022.872007

Lissmann, 1950; Berthe et al., 2009; Hu et al., 2009; Benz et al., 2012; Marvi and Hu, 2012; Abdel-Aal, 2013).

Current snake-inspired robots fail to accurately mimic the locomotion of biological snakes because they neglect the role of frictional interactions in the robot skin design. To enhance the performance of soft slithering robots, we should carefully engineer the friction behavior of the skin of soft robots and synchronize it with the body deformation.

In recent years, inspired by the Japanese art of paper cutting, engineers adopted kirigami to create flexible metasurfaces by perforating an array of cuts into thin elastic sheets to achieve a wide range of mechanically-programmable physical properties (Blees et al., 2015; Lamoureux et al., 2015; Shyu et al., 2015; Zhang et al., 2015; Isobe and Okumura, 2016; Rafsanjani et al., 2017; An et al., 2020; Babaee et al., 2020, 2021; Hong et al., 2022). Stretching kirigami skins triggers elastic instabilities in thin ligaments and transforms the smooth surface of the skin into a 3D texture that has the potential to imbue soft robots with new functionalities (Rafsanjani et al., 2019a). Kirigami lattices on thin elastic sheets are ideal for integrating with elastomeric actuators because they can be designed to deform with the soft actuator. The standard kirigami lattice that allows for stretching of the thin sheet and combined with an extending soft actuator has enabled the soft robots to achieve crawling (Rafsanjani et al., 2018; 2019b), and burrowing (Liu et al., 2019). Altering the kirigami lattice to account for bending as well as elongation and combined with bending soft actuators has enabled soft robots to achieve undulating locomotion (Branyan et al., 2020). Kirigami metasurfaces have also been used as soft grippers (Yang et al., 2021).

The work presented here improves the locomotion of a soft snake robot by implementing an enhanced kirigami pattern that increases the lateral-cranial friction ratio on a snake-inspired skin. Based on results from previous work on a snake-inspired kirigami skinned soft robot (Branyan et al., 2020), we know that increasing frictional anisotropy of the soft snake robot increases the velocity of locomotion. A soft actuator without skin relies on adhesion between the elastomeric material and the surface, rather than sliding friction resulting in isotropic reaction forces. We look to increase the velocity of lateral undulation in this work by controlling the direction of reaction forces from the scales as the body deforms through the design of the lattice of arrayed cuts.

The proposed kirigami design follows a curved pattern, that when wrapped around a soft, fiber-reinforced, bending actuator uses enhanced directional friction to promote slithering of the robot. Bending is achieved by creating a gradient of hinge widths in the lattice pattern, which reduces the overall axial stiffness of the skin when wrapped around an actuator. As the scales rotate laterally (pointing out from the body to the sides) during bending, the anisotropic ratio of friction in the caudal-direction (towards the tail, against the scales) to friction in cranial-direction (towards the head, with the scales) of the system will decrease as fewer scales are oriented along the spine. This trade-off is justified because of biological evidence that lateral reaction forces are necessary for the production of lateral undulation (Hu et al., 2009; Zhang et al., 2021). Biological measurements show a lateral-cranial frictional anisotropy ranging from 1 to 1.72 (Gray and

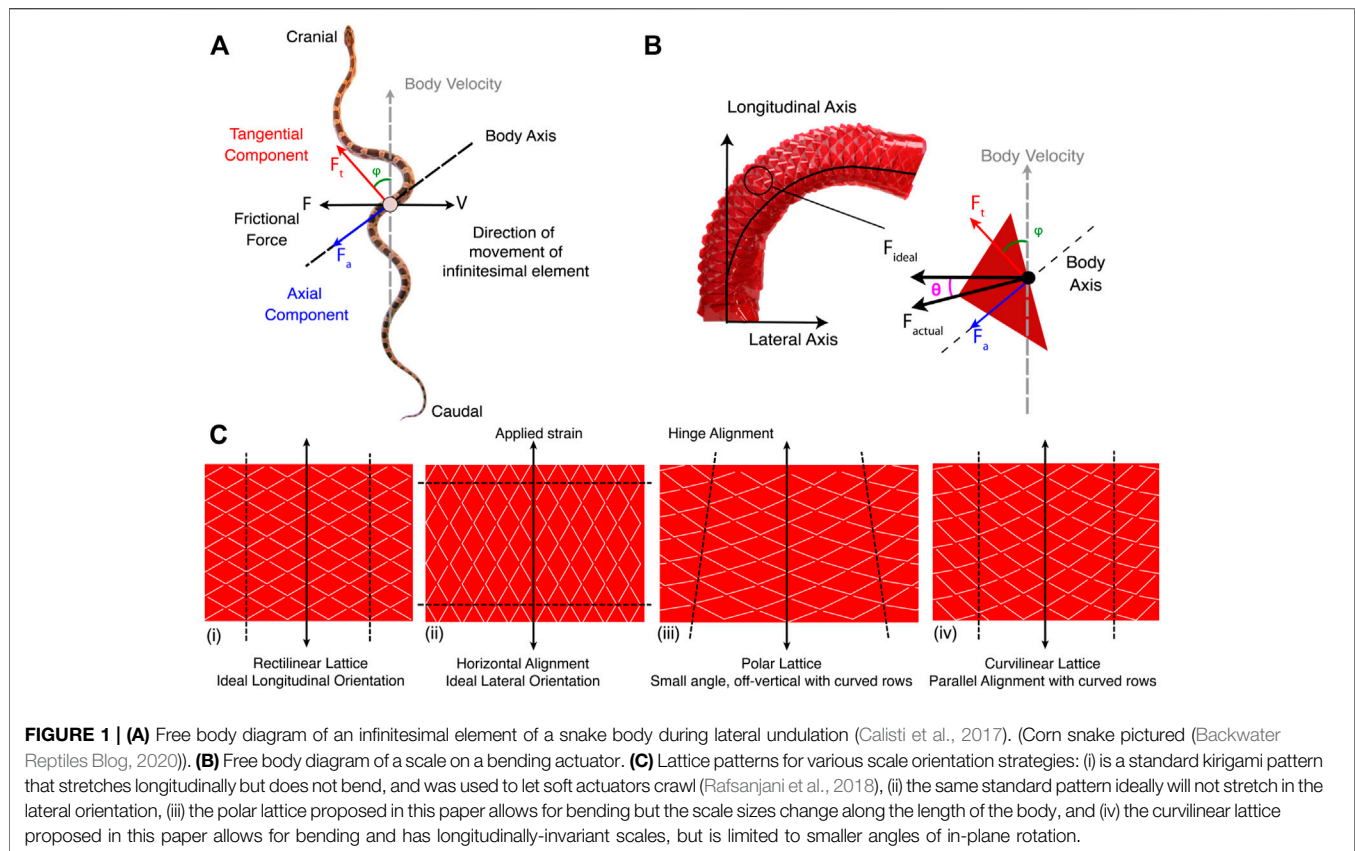
Lissmann, 1950; Berthe et al., 2009; Hu et al., 2009; Benz et al., 2012; Marvi and Hu, 2012; Abdel-Aal, 2013). Thus, we hypothesized that scales approaching the fully lateral orientation would maximize locomotion efficacy of slithering, even at the cost of reduced caudal-cranial frictional anisotropy. To test this prediction, we introduced curved lattices designed to orient the scales laterally to maximize the lateral reaction force, at the cost of decreased longitudinal reaction forces. The resulting locomotion experiments corroborate our hypothesis—the velocity of slithering soft robots is highest with skins that maximize lateral-friction.

2 DESIGN

At their simplest, soft pneumatic actuators are composed of a hyperelastic membrane filled with pressurized fluid. The addition of selectively patterned material directs the isotropic expansion of pressurized gas to do useful anisotropic work. The soft snake robot combines four of these simple fiber-reinforced actuators to form two bidirectional bending actuators that replicate undulatory kinematics. In contrast to its anisotropic kinematics, the isotropic elastomeric skin material (EcoFlex*00–30) does not produce any directional friction forces when in contact with the ground. Any locomotion produced relies on the out-of-phase activation of the two bidirectional bending actuators, and the adhesion between the elastomer and the terrain. Achieving both high absolute lateral friction forces and high caudal-cranial frictional anisotropy through the implementation of a snake-inspired skin greatly increases the velocity of the robot when using lateral undulation. Without a snake-inspired skin, the robot is slow to move across solid surfaces during lateral undulation, and has the tendency to drift sideways.

Lateral undulation is characterized by a traveling sinusoidal wave where an infinitesimal mass element along the sinusoid body is moving in a lateral direction while the overall body velocity is forwards. A free body diagram of an infinitesimal mass element is shown in **Figure 1A**). The friction force felt by the mass element is in the opposite direction of the element's velocity and includes axial and tangential components with respect to the body axis of the snake at that mass element. Forward propagation of the snake is only possible when $F_t \cos \varphi > F_a \sin \varphi$ (Calisti et al., 2017). The micro-mechanics of the interaction between the skin and the terrain is outside the scope of this work, so we assume that the friction force produced by an infinitesimal mass element is in the direction of a single scale tip on the skin. Similar assumptions have been made previously to model and measure contact forces to determine if snakes move their scales to increase friction (Marvi et al., 2016). A free body diagram of the forces acting on a scale is shown in **Figure 1B**). The actual friction force, F_{actual} is along the scale tip and is separated by an angle θ from the ideal friction force vector, F_{ideal} as established in **Figure 1A**). The new kirigami lattices presented in this work were designed to minimize θ so that as

$$\theta \rightarrow 0, F_{\text{actual}} \rightarrow F_{\text{ideal}} \quad (1)$$



Typical kirigami lattices are arranged in a rectilinear grid (**Figure 1Ci**). A rectilinear pattern ensures that the scale tip is always aligned with the body axis of the actuator during locomotion, meaning $\theta = \phi$. Rectilinear lattices still produce useful friction forces that improve the velocity of the robot enacting lateral undulation (Branyan et al., 2020), but there is no tangential component of the friction to optimize interaction during lateral undulation. Since we want to minimize θ , we need a strategy to control the orientation of the scale tips on the skin. The ideal lattice pattern would take the rectilinear pattern and rotate it by 90° as shown in **Figure 1Cii** so the scale tips are pointed laterally to start. However, out-of-plane buckling can only occur if the hinges are mostly aligned with the direction of applied strain. If the scales are oriented 90° from the direction of the applied strain, the hinges cannot buckle, and the scales do not pop out. By patterning the scale tips along a curve rather than a straight line the scale tips can have an initial rotated orientation, that when activated, approaches the ideal friction vector.

Two lattice structures were developed to alter scale orientation: a polar lattice (**Figure 1Ciii**) and a curvilinear lattice (**Figure 1Civ**). The polar lattice is defined by polar coordinates where hinges are located based on an $(R, \theta_{lattice})$ pair. The curvilinear lattice has hinges located along a radius spaced by parallel columns as they are for the rectilinear lattice. A third skin was developed using the curvilinear lattice with an additional circumferential translation of the scale tip to push the

initial orientation further towards the lateral axis (see **Supplementary Figure S1B**). The angle between the ideal friction force vector and the actual vector, θ can then be characterized as a function of the bending angle of the actuator (γ) and the initial scale tip rotation (θ_0) which is a function of the radius of the row (R) and the local circumferential translation (ζ):

$$\theta = f(\gamma, \theta_0(R, \zeta)) \quad (2)$$

A full geometric definition of the kirigami skins can be found in the **Supplementary Material**.

In addition to redefining kirigami skins to allow for ideal scale orientation, we also needed to ensure the new skins allowed for bending of the actuators upon inflation. A basic rectilinear lattice with a triangular scale profile does not allow for bending greater than 10° unless a strategy for decreasing longitudinal stiffness is employed. One simplistic strategy is to make the hinge width as small as possible and the cut profile as large as possible. However, practical material strength constraints limit the implementation of this strategy: if the hinge width is too small, the lattice will easily rip upon contact with a surface. Since the skin is implemented on a robot for practical environmental interactions, the scales need to have a relatively high geometric stiffness when engaged with surface asperities to provide adequate reaction forces to push off against, which decreases with decreasing hinge width. A gradient of hinge

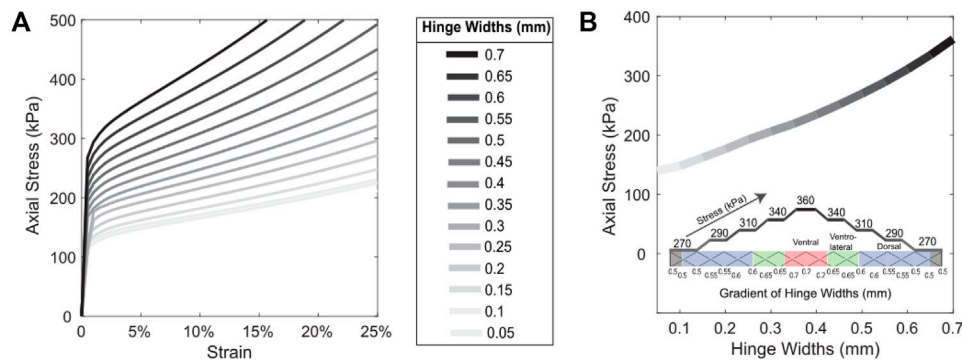


FIGURE 2 | (A) Stress-strain curves for rectilinear lattice and triangular cut profiles at different hinge widths. **(B)** Axial stress across hinge widths used to select hinge widths. The inset shows the hinge width gradient across rectilinear lattice introduced to produce bending.

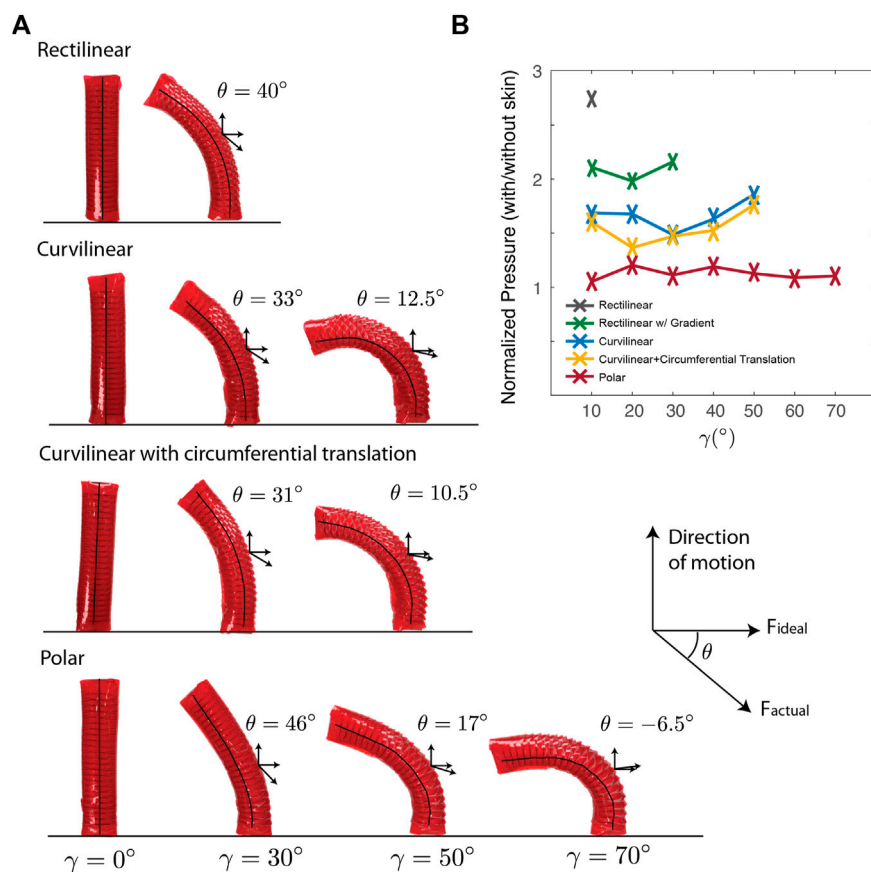


FIGURE 3 | (A) In-plane scale rotation for each skin under bending: (i) rectilinear achieves bending through the non-ideal behavior of the kirigami material that can strain and twist out-of-plane, (ii) curvilinear lattice with inherent hinge gradient, (iii) curvilinear lattice with additional circumferential translation of scale tip further decrease θ , (iv) polar lattice where scales actually over-rotate at the largest bend angle. **(B)** Normalized pressure-bend angle relationship.

widths can be implemented on the rectilinear lattice that has large hinge widths along the bottom of the actuator to ensure stiff scales engage with asperities, but decreases circumferentially to reduce the overall axial stiffness to achieve bending. The gradient is defined by decreasing the

hinge width in the ventro-lateral and dorsal sections of the skin. The curved lattices have an inherent gradient of hinge sizes as well as changes in scale size and shape ensuring bending capabilities without any additional design modifications. We have designed curved lattices to ensure

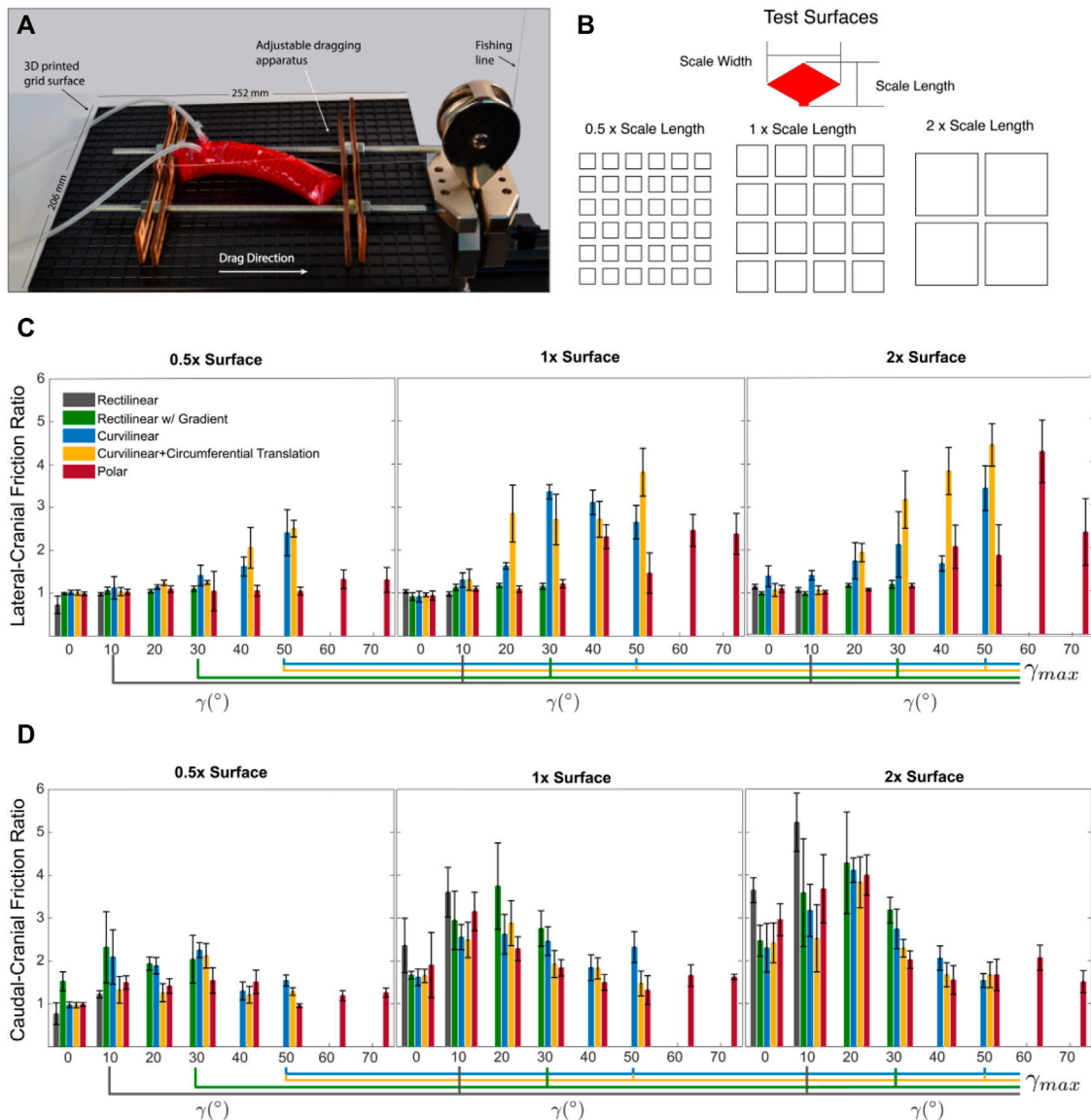


FIGURE 4 | (A) Experimental apparatus for measuring directional friction. Actuator with polar lattice skin on 2x scale length surface. **(B)** Test surface grid spacing normalized by scale length. **(C)** Lateral-cranial friction ratio. **(D)** caudal-cranial friction ratio.

the orientation of scales approach the ideal configuration for maximizing lateral pushing.

3 RESULTS AND DISCUSSION

3.1 Deformation

The stress-strain characterization, determined using finite element analyses, of a rectilinear lattice with triangular scale profiles at different hinge widths is shown in **Figure 2A**. **Figure 2B** shows the stress across hinge widths when strained at 5% which is about half the maximum strain achieved on the skins. These analyses were used to select the hinge widths used in the gradient on the rectilinear lattice shown in the inset of

Figure 2B. Finally, **Figure 3B** shows the normalized pressure-bend angle relationship of the four skins employed. Despite the gradient of hinge widths allowing for bending, the curved lattices, which have a more dramatic gradient of hinge widths and varying scale shape and size, allowed for larger bend angles. The maximum bend angle achieved by the rectilinear lattice was 30°. The curvilinear lattice with and without the additional circumferential translation had a maximum bend angle of 50°, while the polar lattice had a maximum bend angle of 70°. The polar lattice had the most bending due to the large scale size, as well as an axial stiffness gradient caused by increasing the scale size for each additional row of scales. **Figure 3A** shows the difference in angles of the lateral (ideal) vector for each skin type on a scale located in the ventro-lateral section of the skin.

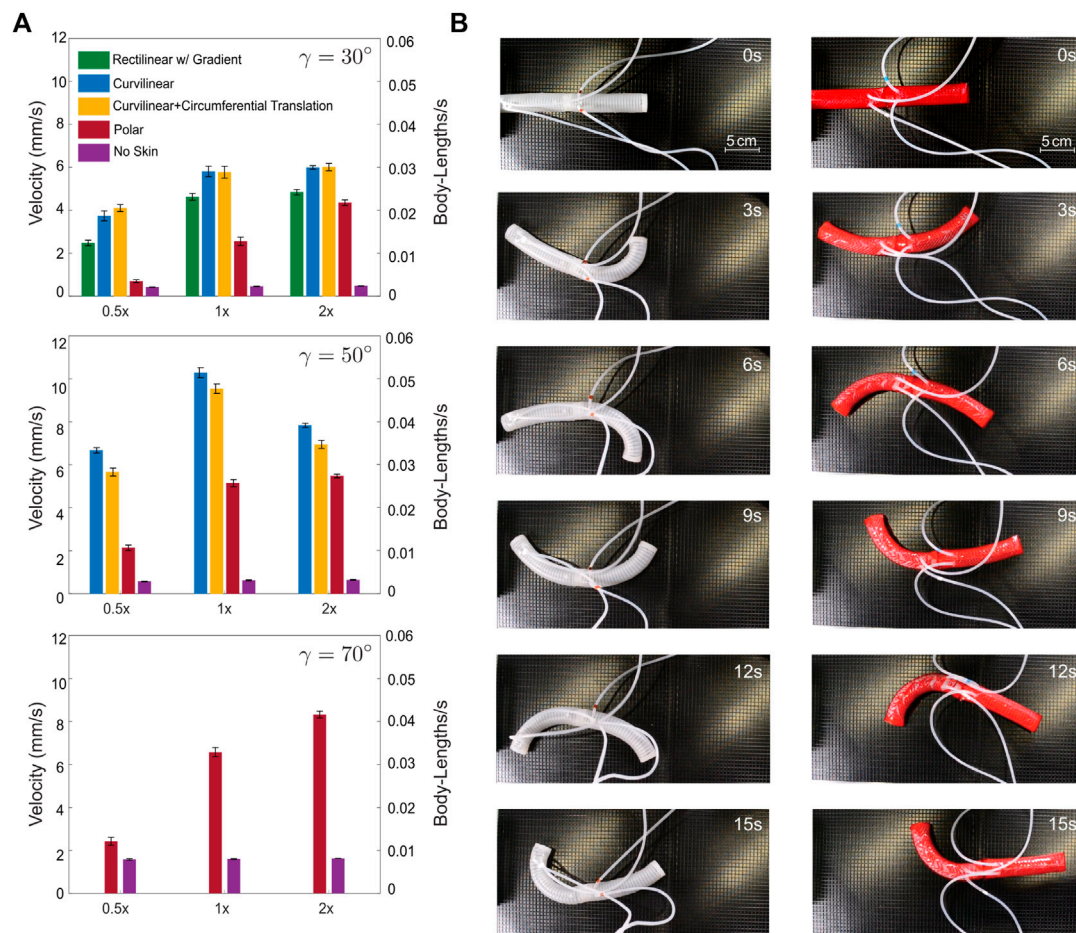


FIGURE 5 | (A) Average velocities of skins on varying surfaces. **(B)** Timelapse of soft snake robot without skin and with curvilinear skin on the 1x surface.

The smaller the angle shown, the more ideal the interaction with the asperity should be for lateral pushing. The curvilinear lattice has the smallest angle, which means it should produce the highest lateral friction. The additional circumferential translation of the scales on the curvilinear lattice resulted in a 2° reduction in the angle of scale rotation which should further increase lateral friction.

3.2 Friction

Directional friction tests (cranial, caudal, and lateral) were performed using a dragging apparatus (see **Figure 4A**) attached to a 10N load cell on a universal testing machine (Mark-10 Corp, NY) with a monofilament nylon cord (0.25 mm, Beadalon®). Friction force was measured by recording the reaction force of the nylon cord against the displacement of the soft actuator wrapped in a kirigami skin as it was dragged across a rough surface. For each skin type, the actuator was inflated and held at a specified pressure corresponding to the desired bend angle. The dragging apparatus was fit to the shape of the actuator by adjusting the position of the lead screws and two planes placed at two extremes of the actuator. The apparatus was positioned such

that it did not drag along the test surface and did not contribute to the drag force measured on the Mark-10. **Figure 4A** shows the actuator in the cranial orientation. The actuator was rotated and the apparatus was refit to measure the caudal and lateral orientations.

3 mm of slack was introduced to the cord at the start of each trial to improve the consistency of the initial stick-slip interaction. All friction tests were performed on three surfaces with a predefined roughness. The surfaces were 3D printed grids (PLA, MeltInk, printed on a LulzBot Taz 6) with walls 1 mm thick and 1 mm deep, and different spacing that is normalized by the scale length of a single kirigami skin scale (4.15 mm). The scale length was the same for each skin tested and determined by the row height (H). The three surface's characteristic spacings were 0.5x (2.075 mm), 1x (4.15 mm), and 2x (8.3 mm) scale length (see **Figure 4B**). As not all skins could enact the same bend angle, each skin was tested in increments of 10° up to its maximum bend angle: 30° for rectilinear with gradient, 50° for curvilinear and curvilinear with the additional circumferential translation, and 70° for polar. This was done to compare the skins against one another, as well as to see how the rotation of scales from bending affected lateral friction.

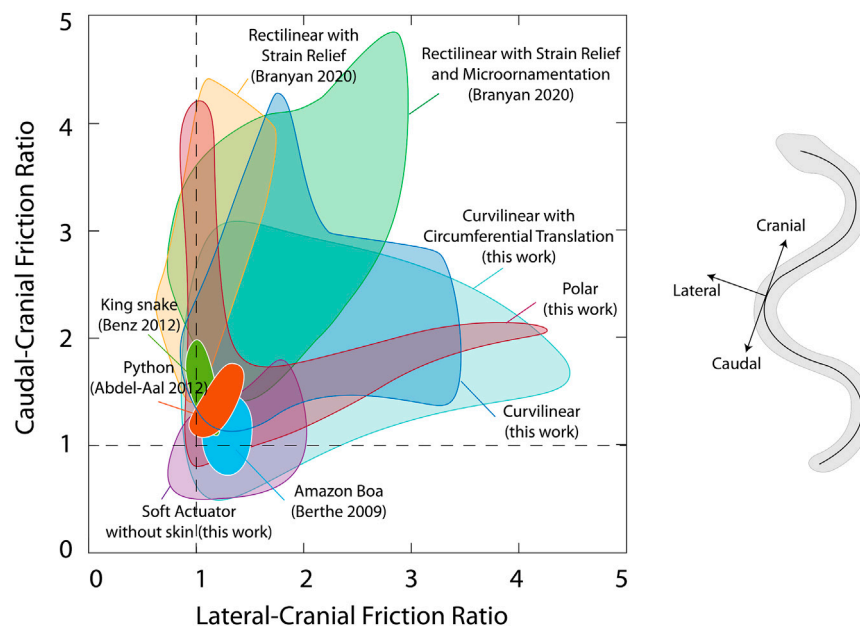


FIGURE 6 | Ashby diagram representing caudal-cranial friction ratio versus lateral-cranial friction ratio for the proposed kirigami skins compared to previous iteration of skin design using microornamentation (Branyan et al., 2020) and biological friction data reported in the literature (Berthe et al., 2009; Benz et al., 2012; Abdel-Aal, 2013)

The caudal:cranial ratio represents the ratio between the caudal (backward) and cranial (forward) drag directions and the lateral-cranial ratio represents the ratio between the lateral and forward drag directions. **Figures 4C,D** show the lateral-cranial and the caudal-cranial friction ratios, respectively. The friction ratios were calculated using the average frictional force measured during dragging after the static friction peak was overcome. We found curvilinear skins (with and without additional circumferential translation) produced the highest lateral-cranial friction ratios across all surfaces. The additional 2° of scale rotation achieved by circumferential translation resulted in an increase in frictional force compared to the plain curvilinear skins, especially on the larger asperities.

The polar skin, although having scale rotation approaching the ideal vector for lateral pushing did not perform well (friction ratios did not exceed 1.5 on average) on small grid-spacing (asperities were $0.5\times$ the length of the skin scales). Despite the scales having the same length as one another, the width of the scale limited how many scales could engage with asperities. The ventral portion of the polar skin only had one column of scales interacting with the ground whereas the rectilinear and curvilinear skins had three or more columns. We infer that the more scales are in contact with the surface at a time, the higher the friction force.

The curvilinear lattices produced a much higher lateral-cranial friction ratio compared to the rectilinear lattice that had no explicit design intent for increasing lateral resistance. The polar lattice, when on the $2\times$ surface with asperities large enough to engage with, also produced high lateral-cranial

ratios at high bend angles. Therefore, the curved lattices, designed to orient the scale tips closer to the ideal vector for lateral pushing, were successful in increasing lateral resistance.

As expected, the rectilinear skin had the highest caudal-cranial friction ratio (exceeding 5:1) as there were more scales pointed longitudinally with respect to the surface asperities. The curved lattices make a trade off to increase lateral friction by decreasing caudal-cranial anisotropy. Despite decreasing the number of scales oriented axially for longitudinal pushing, the curved lattices still marginally exceeded a 1:1 ratio for caudal-cranial anisotropy. Future work could evaluate how the number of anchor points (scales in contact with surface asperities) affects the resulting frictional forces.

3.3 Locomotion

Locomotion experiments were performed at each of the maximum bend angles achieved by the different skins and compared to a robot with no skin on all three surfaces. The gait parameters driving lateral undulation are frequency of bending, and amplitude of the bend. The frequency was held constant across all tests. The amplitude was adjusted for each skin to drive the actuators to the desired bend angle determined in **Figure 3**. Motion capture data was collected by the OptiTrack Prime 13 system (Natural Point Inc.) and used to calculate the velocity of the robot. The average velocity of the robot with each skin is shown in **Figure 5A**.

Based on the locomotion results, we found that the production of lateral resistance, even to the detriment of the caudal-cranial frictional anisotropy, proved vital in increasing velocity. The curvilinear lattices, which had good rotation of

scales and good geometric stiffness of scales (based on our tangible and visual observations) performed best. The polar lattice was not effective on the surfaces with small asperities, so it performed best on the 2x surface, but still had a maximum velocity less than that of the curvilinear skins. Maximizing bend angle maximizes velocity. Despite only bending to 50°, the curvilinear skin increased the velocity of a robot with no skin by 530% at its maximum velocity which occurred on the 1x surface (time-lapse shown in **Figure 5B**). Comparing to the rectilinear skin at 30°, both the rectilinear and curvilinear skins did best on the 2x surface with a 25% increase in velocity of the curvilinear skin over the rectilinear skin.

Figure 6 shows an Ashby plot comparing the frictional ratios of the new curved lattice skins, the skin developed previously in (Branyan et al., 2020), and friction measurements on biological snakes from the literature (Berthe et al., 2009; Benz et al., 2012; Abdel-Aal, 2013). This information can be used to select an appropriate skin for the desired frictional properties. Ideally, any skin on a limbless robot should employ frictional ratios greater than 1. If the selected gait is lateral undulation, where lateral resistance is necessary, targeting larger lateral-cranial ratios is best based on the experiments performed in this work.

4 CONCLUSION

Lateral friction is crucial for lateral undulation in biological snakes Hu et al. (2009). However, in existing snake-inspired robots, other than using wheels, no other mechanism has been proposed to increase lateral resistance over caudal-cranial anisotropy. We introduced here a set of curved kirigami skins that take advantage of the kinematics of bending to orient 3D structures to produce higher lateral reaction forces when engaged with surface asperities. Unlike the typical rectilinear grid pattern, the array of cuts embedded in the curvilinear kirigami skins were arranged along a curve. By using curved rows, the tips of the scales were oriented more laterally, such that bending, of the body would bring the scales further into alignment with the ideal lateral force vector. The curved design also introduced a gradient of hinge widths which reduced the overall axial stiffness of the skin, further facilitating body-bending when wrapped around a soft bending actuator.

We showed when more scales point laterally (minimizing θ), a higher lateral reaction force upon contact with an asperity is achieved. The angle of scale rotation coupled with the size and geometric stiffness of the scale drives the locomotion performance. It was found that the curvilinear skins produced the highest speed, improving the velocity over a robot with no skin by 530%. Though the curvilinear skins could not produce as much bending as the polar skin, they accommodated more scales

on the ventral portion of the robot to engage with the surface, thus, increasing its overall locomotion efficiency.

In the polar skin, because of the gradient of scale sizes along the longitudinal axis, a non-uniform curvature emerges. This shows how kirigami skins can be used to drive not only the interaction between a robot and its environment, but the kinematics of the robot itself. Work on using kirigami lattice patterns to drive the shape of soft inflatable bladders has been recently introduced (Jin et al., 2020). Future work in using kirigami to drive both the behavior and interaction of soft actuators could greatly reduce the manufacturing effort on the soft actuator side. Kirigami skins can be tailored to achieve the desired kinematics and interaction dynamics necessary to produce the targeted behavior when wrapped around any soft inflatable bladder. Ultimately, we consider this work as contributing to the broader design knowledge of body-skin-environment interactions which will mediate soft robotic performance in potential applications ranging from medical implants to warehouse material handling to planetary surface exploration.

DATA AVAILABILITY STATEMENT

The original contributions presented in the study are included in the article/**Supplementary Material**, further inquiries can be directed to the corresponding author.

AUTHOR CONTRIBUTIONS

CB, YM, and RH designed the research. CB designed and developed the kirigami skin and soft actuators, and performed all experiments. AR and KB contributed to the kirigami models. CB, AR, KB, RH, and YM wrote the manuscript.

FUNDING

This work was supported by the National Science Foundation (award IIS-1734627) and the Office of Naval Research Young Investigator Program (ONR YIP N00014-16-1-2529; P.O Tom McKenna).

SUPPLEMENTARY MATERIAL

The Supplementary Material for this article can be found online at: <https://www.frontiersin.org/articles/10.3389/frobt.2022.872007/full#supplementary-material>

REFERENCES

- Abdel-Aal, H. A. (2013). On Surface Structure and Friction Regulation in Reptilian Limbless Locomotion. *Journal of the Mechanical Behavior of Biomedical Materials* 22, 115–135. doi:10.1016/j.jmbbm.2012.09.014

- An, N., Domel, A. G., Zhou, J., Rafsanjani, A., and Bertoldi, K. (2020). Programmable Hierarchical Kirigami. *Adv. Funct. Mater.* 30, 1906711. doi:10.1002/ADFM.201906711
- Babaei, S., Pajovic, S., Rafsanjani, A., Shi, Y., Bertoldi, K., and Traverso, G. (2020). Bioinspired Kirigami Metasurfaces as Assistive Shoe Grips. *Nat Biomed Eng* 4, 778–786. doi:10.1038/s41551-020-0564-3

- Babaei, S., Shi, Y., Abbasalizadeh, S., Tamang, S., Hess, K., Collins, J. E., et al. (2021). Kirigami-inspired Stents for Sustained Local Delivery of Therapeutics. *Nat. Mater.* 20, 1085–1092. doi:10.1038/s41563-021-01031-1
- Backwater Reptiles Blog (2020). *Most Popular Corn Snake Morphs*. Rocklin, CA: Backwater Reptiles Blog.
- Benz, M. J., Kovalev, A. E., and Gorb, S. N. (2012). “Anisotropic Frictional Properties in Snakes,” in *Bioinspiration, Biomimetics, and Bioreplication 2012*. Editor A. Lakhtakia (Bellingham, Washington, USA: SPIE), Vol. 8339, 83390X. doi:10.1117/12.916972
- Berthé, R. A., Westhoff, G., Bleckmann, H., and Gorb, S. N. (2009). Surface Structure and Frictional Properties of the Skin of the Amazon Tree boa *Corallus hortulanus* (Squamata, Boidae). *J. Comp. Physiol. A* 195, 311–318. doi:10.1007/s00359-008-0408-1
- Blees, M. K., Barnard, A. W., Rose, P. A., Roberts, S. P., McGill, K. L., Huang, P. Y., et al. (2015). Graphene Kirigami. *Nature* 524, 204–207. doi:10.1038/nature14588
- Branyan, C., Fleming, C., Remaley, J., Kothari, A., Tumer, K., Hatton, R. L., et al. (2017). “Soft Snake Robots: Mechanical Design and Geometric Gait Implementation,” in 2017 IEEE International Conference on Robotics and Biomimetics (ROBIO) (Macau, Macao: IEEE), 282–289. doi:10.1109/ROBIO.2017.8324431
- Branyan, C., Hatton, R. L., and Menguc, Y. (2020). Snake-Inspired Kirigami Skin for Lateral Undulation of a Soft Snake Robot. *IEEE Robot. Autom. Lett.* 5, 1728–1733. doi:10.1109/lra.2020.2969949
- Calisti, M., Picardi, G., and Laschi, C. (2017). Fundamentals of Soft Robot Locomotion. *J. R. Soc. Interface* 14, 20170101. doi:10.1098/rsif.2017.0101
- Crespi, A., and Jan Ijspeert, A. (2006). “AmphiBot II: An Amphibious Snake Robot that Crawls and Swims Using a Central Pattern Generator,” in Proceedings of the 9th International Conference on Climbing and Walking Robots, 19–27.
- Gans, C. (1962). Terrestrial Locomotion without Limbs. *Am. Zool.* 2, 167–182. doi:10.1093/icb/2.2.167
- Gray, J., and Lissmann, H. W. (1950). The Kinetics of Locomotion of the Grass-Snake. *Journal of Experimental Biology* 26, 354–367. doi:10.1242/jeb.26.4.354
- Hirose, S. (1993). *Biologically Inspired Robots (Snake-like Locomotor and Manipulator)*. Oxford: Oxford University Press.
- Hong, Y., Chi, Y., Wu, S., Li, Y., Zhu, Y., and Yin, J. (2022). Boundary Curvature Guided Programmable Shape-Morphing Kirigami Sheets. *Nat. Commun.* 13. doi:10.1038/s41467-022-28187-x
- Hu, D. L., Nirody, J., Scott, T., and Shelley, M. J. (2009). The Mechanics of Slithering Locomotion. *Proc. Natl. Acad. Sci. U.S.A.* 106, 10081–10085. doi:10.1073/pnas.0812533106
- Isobe, M., and Okumura, K. (2016). Initial Rigid Response and Softening Transition of Highly Stretchable Kirigami Sheet Materials. *Sci. Rep.* 6, 24758. doi:10.1038/srep24758
- Jin, L., Forte, A. E., Deng, B., Rafsanjani, A., and Bertoldi, K. (2020). Kirigami-Inspired Inflatables with Programmable Shapes. *Adv. Mater.* 32, 2001863. doi:10.1002/adma.202001863
- Lamoureux, A., Lee, K., Shlian, M., Forrest, S. R., and Shtein, M. (2015). Dynamic Kirigami Structures for Integrated Solar Tracking. *Nat. Commun.* 6, 8092. doi:10.1038/ncomms9092
- Liu, B., Ozkan-Aydin, Y., Goldman, D. I., and Hammond, F. L., III (2019). “Kirigami Skin Improves Soft Earthworm Robot Anchoring and Locomotion under Cohesive Soil,” in IEEE International Conference on Soft Robotics, 828–833. doi:10.1109/robosoft.2019.8722821
- Marvi, H., Cook, J. P., Streater, J. L., and Hu, D. L. (2016). Snakes Move Their Scales to Increase Friction. *Biotribology* 5, 52–60. doi:10.1016/j.biotri.2015.11.001
- Marvi, H., and Hu, D. L. (2012). Friction Enhancement in Concertina Locomotion of Snakes. *J. R. Soc. Interface* 9, 3067–3080. doi:10.1098/rsif.2012.0132
- Onal, C. D., and Rus, D. (2013). Autonomous Undulatory Serpentine Locomotion Utilizing Body Dynamics of a Fluidic Soft Robot. *Bioinspir. Biomim.* 8, 026003–026010. doi:10.1088/1748-3182/8/2/026003
- Rafsanjani, A., Bertoldi, K., and Studart, A. R. (2019a). Programming Soft Robots with Flexible Mechanical Metamaterials. *Sci. Robot.* 4, 7874. doi:10.1126/scirobotics.aav7874
- Rafsanjani, A., Bertoldi, K., and Paulson, J. A. (2017). Buckling-Induced Kirigami. *Phys. Rev. Lett.* 118. doi:10.1103/PhysRevLett.118.084301
- Rafsanjani, A., Jin, L., Deng, B., and Bertoldi, K. (2019b). Propagation of Pop Ups in Kirigami Shells. *Proc. Natl. Acad. Sci. U.S.A.* 116, 8200–8205. doi:10.1073/pnas.1817763116
- Rafsanjani, A., Zhang, Y., Liu, B., Rubinstein, S. M., and Bertoldi, K. (2018). Kirigami Skins Make a Simple Soft Actuator Crawl. *Sci. Robot.* 3, eaar7555. doi:10.1126/scirobotics.aar7555
- Shyu, T. C., Damasceno, P. F., Dodd, P. M., Lamoureux, A., Xu, L., Shlian, M., et al. (2015). A Kirigami Approach to Engineering Elasticity in Nanocomposites through Patterned Defects. *Nature Mater.* 14, 785–789. doi:10.1038/nmat4327
- Yang, Y., Vella, K., and Holmes, D. P. (2021). Grasping with Kirigami Shells. *Science Robotics* 6, abd6426. doi:10.1126/scirobotics.abd6426
- Zhang, X., Naughton, N., Parthasarathy, T., and Gazzola, M. (2021). Friction Modulation in Limbless, Three-Dimensional Gaits and Heterogeneous Terrains. *Nat. Commun.* 12, 1–8. doi:10.1038/s41467-021-26276-x
- Zhang, Y., Yan, Z., Nan, K., Xiao, D., Liu, Y., Luan, H., et al. (2015). A Mechanically Driven Form of Kirigami as a Route to 3D Mesoscale Structures in Micro/nanomembranes. *Proc. Natl. Acad. Sci. U.S.A.* 112, 11757–11764. doi:10.1073/pnas.1515602112

Conflict of Interest: The authors declare that the research was conducted in the absence of any commercial or financial relationships that could be construed as a potential conflict of interest.

Publisher's Note: All claims expressed in this article are solely those of the authors and do not necessarily represent those of their affiliated organizations, or those of the publisher, the editors and the reviewers. Any product that may be evaluated in this article, or claim that may be made by its manufacturer, is not guaranteed or endorsed by the publisher.

Copyright © 2022 Branyan, Rafsanjani, Bertoldi, Hatton and Mengüç. This is an open-access article distributed under the terms of the Creative Commons Attribution License (CC BY). The use, distribution or reproduction in other forums is permitted, provided the original author(s) and the copyright owner(s) are credited and that the original publication in this journal is cited, in accordance with accepted academic practice. No use, distribution or reproduction is permitted which does not comply with these terms.

Supplementary Material

1 LATTICE GEOMETRY

The definitions of the three lattices are shown in Fig. S1a. Algorithms used to generate the hinge locations for each lattice can be found below. The rectilinear lattice refers to the typical kirigami lattice structure of a parallel grid aligning the hinges and profiles with the direction of the applied axial strain. As this is the standard kirigami pattern, there is no strategy for increasing lateral friction other than the rotation of the scales with respect to surface asperities inherent upon the bending of the actuator. This lattice is defined by a lattice length, L , lattice angle, ϕ , and a hinge width, δ . The geometric relationship between these parameters result in a uniform column width, $W = l \cos(\phi/2)$ and a row height of scales $H = l \sin(\phi/2)$. The hinge locations can be identified by (x, y) coordinates based on the values of the described parameters. Since we are comparing this standard kirigami lattice to our newly created lattices, maintaining consistent parameter values is necessary. The following lattices are built based on these described parameter values.

The polar lattice is defined by polar coordinates rather than rectilinear coordinates. A radius R defines the shape of the rows which are offset by the same row height H defined by the rectilinear lattice. An angle, $\theta_{lattice}$ defines the orientation and spacing of the columns. The hinge locations are defined by the $(R, \theta_{lattice})$ coordinates. An additional parameter, K , defines a negative y-displacement from the origin (center, bottom of the lattice pattern shown in Fig S1a). of the polar lattice in which to define the center point of the radius. This is necessary because as you move axially along the lattice, the columns get closer together. This parameter K controls the smallest and largest scale size along the length of the lattice. The lower bound of K is limited by the point at which scales will intersect one another, and the lattice structure would breakdown. The change in scale size along the skin complicates our implementation of a soft snake robot as this creates a gradient of stiffness along the longitudinal axis which results in non-constant curvature. More importantly, the larger the scale, the less stiff it is, so interactions with an asperity on a surface will be relatively weak as the scale size increases. The specific micro-mechanics of asperity-scale interaction is beyond the scope of the current work, but opens up intriguing new mechanical design questions, as detailed in the discussion and conclusion.

The curvilinear lattice is a combination of the rectilinear and polar lattices. To prevent the change in scale size along the skin as is apparent with the polar lattice, the parallel columns from the rectilinear lattice were maintained while curved rows from the polar lattice were implemented. The rows of scales are defined by a radius, R and the columns are defined by the same column width W from the rectilinear lattice. Hinge locations are defined by the intersection of the radius, with the parallel columns.

As the goal is to maximize lateral friction by orienting the scales as close to lateral as possible, an additional circumferential translation of the scale tips was implemented on the curvilinear lattice and is defined by arc angle $\zeta = 5^\circ$ as shown in Fig. S1b. As the ventral and part of the ventro-lateral portions of the skin are the only parts in contact with surface asperities, that was the only area of the curvilinear lattice where additional scale tip circumferential translations were implemented. Performing a circumferential translation of the scales caused a decrease in hinge width that would lead to the intersection of cuts if

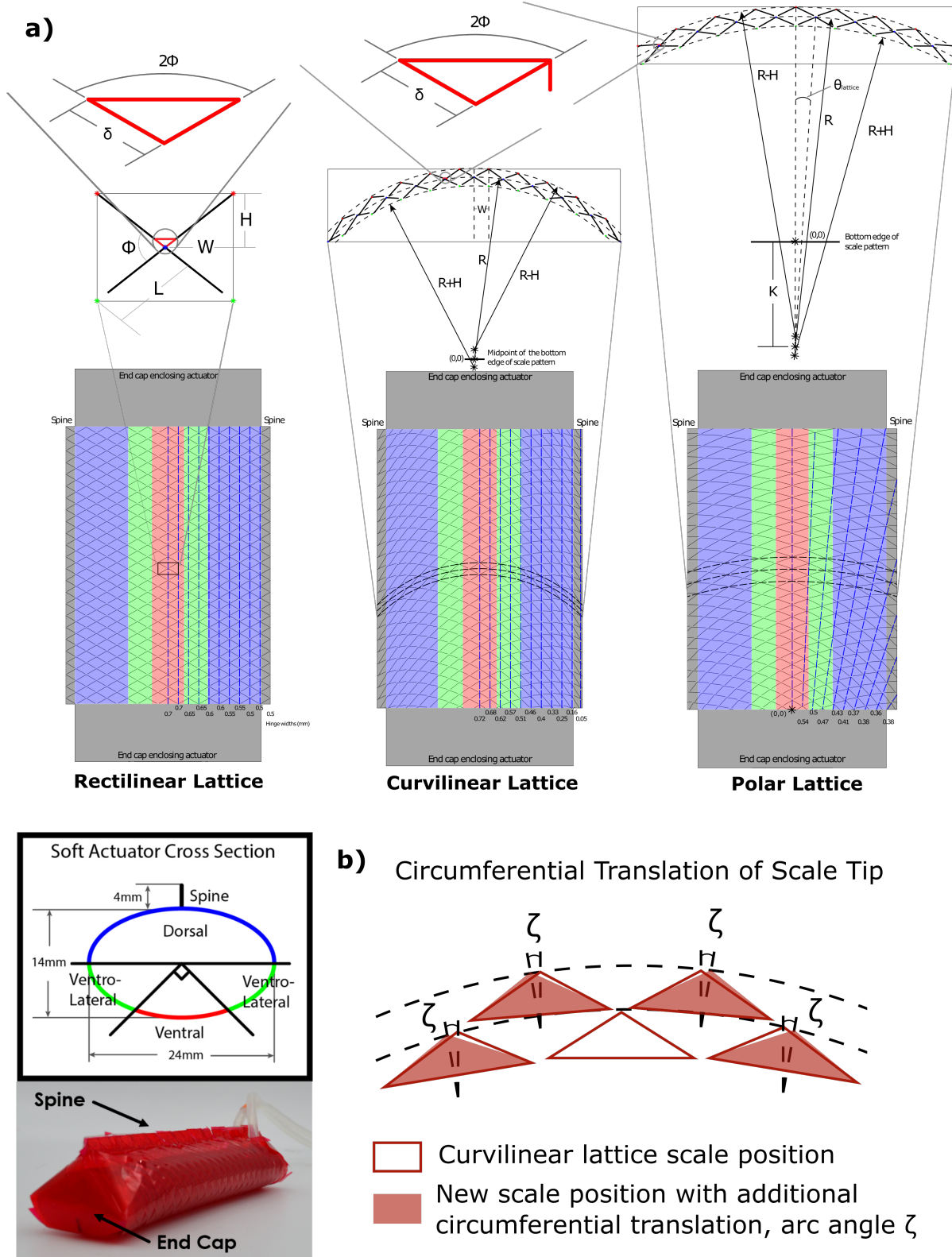


Figure S1: **a)** Kirigami lattice patterns with broken out unit cell and hinge definitions. **b)** Additional circumferential translation parameter used on curvilinear lattice to further push scale tip towards lateral ideal.

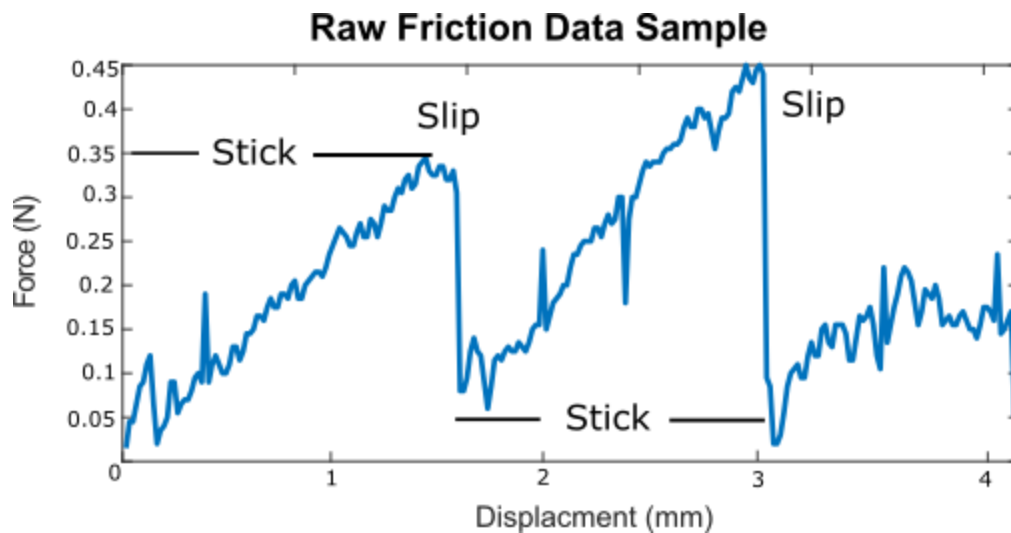


Figure S2: Plot of raw data collected from drag experiments to determine friction of skins on actuator.

propagated across the entire width of the skin. By keeping the additional circumferential translation of the scales to high interaction locations, the integrity of the skin is maintained.

2 FRICTION DATA PROCESSING

The drag experiments described in the manuscript resulted in force vs. displacement data. This experimental data was used to calculate friction in the cranial, caudal, and lateral directions of the skin as it was pulled across a rough surface. The scales on the skin would engage with an asperity on the surface producing high reaction forces until a maximum was reached and the scale disengaged from the asperity. This results in a stick-slip phenomenon. The plot in Fig. S2 shows a sample of the force-displacement data collected illustrating stick-slip. We took the average over several iterations of stick-slip as a way to estimate dynamic friction. We then took the average over ten trials for each skin, bend angle, and surface combination. The caudal friction data was divided by the cranial friction data for each combination to produce the caudal:cranial friction ratio. The same was done for the lateral friction data to produce the lateral:cranial ratio.

3 FRICTION RATIO WITH ROBOT WITHOUT SKIN

The plots shown in Fig. S3 provide a comparison of the frictional ratios of the skins designed in this work with a robot without skin. It is difficult to make a direct comparison because the surface interaction of the robot without skin is adhesion, which relies on surface area engagement. As seen in the plots, there is no frictional anisotropy (ratios greater than 1) present in the robot without skin for the caudal-cranial ratio. The lateral-cranial ratio shows some frictional anisotropy for the lower bend angles because more of the surface was oriented perpendicular to the drag direction. Due to the effects of adhesion, this increased the drag force of the robot as it was pulled across the test surface. Biological snakes rely on sliding friction as their primary surface interaction which is what motivated this work. The skins were designed to remove any effects from adhesion, and introduce frictional anisotropy present on biological snake skin.

4 ALGORITHMS

The algorithms shown below outline the method for generating the hinge locations for both the unit cell, and the full lattice, of each lattice type. The values of R and $\theta_{lattice}$ are used to determine which lattice

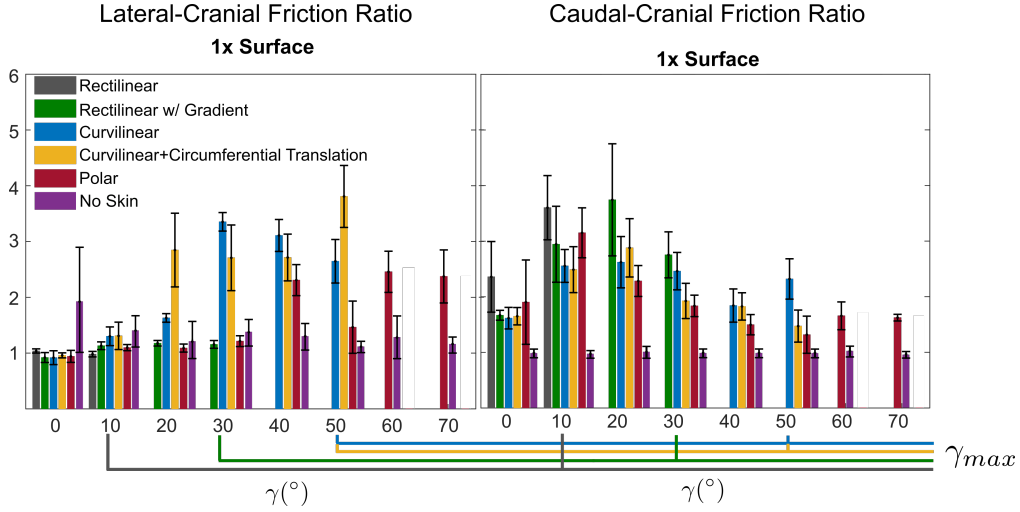


Figure S3: Plots of anisotropic friction ratios including robot without skin

is being used. If $R \rightarrow \infty$ that implies that the rows are horizontal lines rather than radii, and therefore reference the typical rectilinear lattice. Any other value of R can be used to generate one of the curved lattices. $\theta_{lattice}$ is then used to determine whether the desired lattice is curvilinear or polar. If $\theta_{lattice} = 0$ then that means the columns are vertical as they are in the rectilinear lattice, which then determines that the desired lattice is curvilinear. Any other value of $\theta_{lattice}$ can be used to generate the polar lattice.

4.1 Notes for Algorithms 2 and 3

Nested FOR loops, as used for the polar lattice algorithm, can be used for patterning the unit cells for the other two lattices. We left them broken out here to emphasize how the unit cell is defined. Using the nested FOR loops simplifies the definition of the `Middle_Hinges[1](X,Y)` as the first (X,Y) pair in the `Middle_Hinges` array is the center point of the unit cell that then gets translated to make the rest of the tessellated structure. However, leaving the unit cell as a separate definition helps to show that only the curvilinear and rectilinear lattices have unit cells whereas the polar lattice does not.

4.2 Notes for Algorithms 3 and 4

The curvilinear lattice is a hybrid of the rectilinear lattice and the polar lattice. That means that the linear columns from the rectilinear lattice are maintained with curvilinear rows. Because we started with the rectilinear lattice, we carry over the column and row spacing as defined there ($X_{off} = 2l \cos(\phi/2)$ and $Y_{off} = l \sin(\phi/2)$) to compare them directly in use on the robot. However, this is arbitrary. Both the column and row spacing can be chosen at will. The rectilinear lattice is defined by a lattice width l and lattice angle ϕ , which then define the column and row spacing. The selection of l and ϕ is arbitrary though. There is no reason the column and row spacing have to be the same across lattices, that's just what we did to make a proper comparison in performance. For those not starting from the rectilinear lattice, using l and ϕ doesn't make sense. Instead, X_{off} and Y_{off} values can be defined directly. This is also true for the polar lattice which departs even further from the original rectilinear lattice strategy.

Algorithm 1: Hinge Locations for all Lattices**Input:** $l, \phi, R, \theta_{lattice}, M, N, K$ **Output:** (X,Y) Coordinates for the hinge locations for selected lattice**Parameters**

l = lattice spacing ϕ = lattice angle
 R = radius $\theta_{lattice}$ = angle between columns
 M = skin width N = skin length
 K = negative y-displacement from origin for center of radii
 $X_{off} = 2l \cos(\phi/2)$: distance between columns
 $Y_{off} = l \sin(\phi/2)$: distance between rows

(X,Y) Output Arrays

Top_Hinges [] : array of hinge locations for middle row
 Middle_Hinges [] : array of hinge locations for middle row
 Bottom_Hinges [] : array of hinge locations for middle row

```

if  $\theta_{lattice} = 0$  &&  $R \rightarrow \infty$  then
  | rectilinear_lattice( $X_{off}, Y_{off}, M, N$ )
end

if  $\theta_{lattice} = 0$  then
  | curv_lattice( $R, X_{off}, Y_{off}, M, N$ )
end

else
  | pol_lattice( $R, \theta_{lattice}, Y_{off}, M, N, K$ )
end
  
```

Algorithm 2: rectilinear_lattice (X_{off}, Y_{off}, M, N)**Result:** (X,Y) Coordinates for the hinge locations on the rectilinear lattice**Unit Cell Definition**

Middle Hinge [1] = (0 , 0)
 Top_Hinges [1] = ($X_{off}/2, Y_{off}$);
 Top_Hinges [2] = ($-1 * X_{off}/2, Y_{off}$);
 Bottom_Hinges [1] = ($X_{off}/2, -1 * Y_{off}$);
 Bottom_Hinges [2] = ($-1 * X_{off}/2, -1 * Y_{off}$);

Pattern unit cells along width and length of skin

```

for  $m = 1:M$  (rounded to nearest integer) do
  | for  $n = 1:N$  (rounded to nearest integer) do
    | | (Middle_Hinges [1]_X +=  $X_{off} * m$ , Middle_Hinges [1]_Y +=  $2Y_{off} * n$ );
  | end
end
  
```

Algorithm 3: $\text{curv_lattice}(R, X_{\text{off}}, Y_{\text{off}}, M, N)$ **Result:** (X,Y) Coordinates for the hinge locations on the curvilinear lattice**Unit Cell Definition**

Middle_Hinges [1] = (0 , r)

for $i = 1:1/2M / X_{\text{off}}$ (rounded to nearest integer) **do**Middle_Hinges_Right [i+1] = $(X_{\text{off}} * i, \sqrt{R^2 - (X_{\text{off}} * i)^2})$;Middle_Hinges_Left [i+1] = $(-X_{\text{off}} * i, \sqrt{R^2 - (X_{\text{off}} * i)^2})$;Top_Hinges_Right [i+1] = $(X_{\text{off}} * i - X_{\text{off}}/2, \sqrt{R^2 - (X_{\text{off}} * i - X_{\text{off}}/2)^2} + Y_{\text{off}})$;Top_Hinges_Left [i+1] = $(-X_{\text{off}} * i - X_{\text{off}}/2, \sqrt{R^2 - (X_{\text{off}} * i - X_{\text{off}}/2)^2} + Y_{\text{off}})$;Bottom_Hinges_Right [i+1] = $(X_{\text{off}} * i - X_{\text{off}}/2, \sqrt{R^2 - (X_{\text{off}} * i - X_{\text{off}}/2)^2} - Y_{\text{off}})$;Bottom_Hinges_Left [i+1] = $(-X_{\text{off}} * i - X_{\text{off}}/2, \sqrt{R^2 - (X_{\text{off}} * i - X_{\text{off}}/2)^2} - Y_{\text{off}})$;**end**

Middle_Hinges = [Middle_Hinges_Right Middle_Hinges_Left];

Top_Hinges = [Top_Hinges_Right Top_Hinges_Left];

Bottom_Hinges = [Bottom_Hinges_Right Bottom_Hinges_Left];

Pattern unit cells along length of skin**for** $i = 1:N$ (rounded to nearest integer) **do**| (Middle_Hinges [1]-X, Middle_Hinges [1]-Y += $2 * Y_{\text{off}}$);**end****Algorithm 4:** $\text{pol_lattice}(R, \theta_{\text{lattice}}, Y_{\text{off}}, M, N, K)$ **Result:** (X,Y) Coordinates for the hinge locations on the polar lattice**Full lattice pattern generation (unit cell undefinable)****for** $n = 0:N$ (round to nearest integer) **do**R = $R + Y_{\text{off}} * n$;**for** $m = 0:1/2M / R \sin \theta_{\text{lattice}}$ (rounded to nearest integer) **do**

i = odd numbered m's;

Middle_Hinges_Right [m] =

 $((R - Y_{\text{off}}) \sin(\theta_{\text{lattice}}/2 * i), (R - Y_{\text{off}}) \cos(\theta_{\text{lattice}}/2 * i) - K)$;

Middle_Hinges_Left [m] =

 $((R - Y_{\text{off}}) \sin(-\theta_{\text{lattice}}/2 * i), (R - Y_{\text{off}}) \cos(\theta_{\text{lattice}}/2 * i) - K)$;Top_Hinges_Right [m+1] = $(R \sin(\theta_{\text{lattice}} * m), R \cos(\theta_{\text{lattice}} * m) - K)$;Top_Hinges_Left [m+1] = $(R \sin(-\theta_{\text{lattice}} * m), R \cos(\theta_{\text{lattice}} * m) - K)$;

Bottom_Hinges_Right [m+1] =

 $((R - Y_{\text{off}} * 2) \sin(\theta_{\text{lattice}} * m), (R - Y_{\text{off}} * 2) \cos(\theta_{\text{lattice}} * m) - K)$;

Bottom_Hinges_Left [m+1] =

 $((R - Y_{\text{off}} * 2) \sin(-\theta_{\text{lattice}} * m), (R - Y_{\text{off}} * 2) \cos(\theta_{\text{lattice}} * m) - K)$;**end****end**

Middle_Hinges = [Middle_Hinges_Right Middle_Hinges_Left];

Top_Hinges = [Top_Hinges_Right Top_Hinges_Left];

Bottom_Hinges = [Bottom_Hinges_Right Bottom_Hinges_Left];